7.1

ATMOSPHERIC TURBULENT FLUX OBSERVATION ON THE TIDAL ZONE OVER THE ARIAKE SEA JAPAN

Kenji Tanaka*
Kumamoto University, Kumamoto, Japan

1. INTRODUCTION

The Ariake Sea is a typical closed bay on the west coast of Kyushu Island, Japan (Fig. 1). The Ariake Sea has a dynamic tidal range, reaching more than 5 m in the closed-off section of the bay at the spring tide. The region also hosts a vast tidal flat that exposes an area of larger than 200 km^2 at the spring tide, representing about 40% of the total exposed tidal area of Japan. Several of the exposed coastal regions in the Ariake Sea extend for more than 1–2 km offshore depending on the tidal fluctuation.

The atmospheric turbulence over this inter-tidal zone has been thought to play an important role in driving the current (or wave) field and the circulation of subsidence accompanying the seawater current in sea regions. Many observational and numerical studies have been conducted in recent years on the atmospheric boundary layer in many areas including coastal regions (e.g., Plant et al., 2003; Kruit et al., 2004; Lange et al, 2004). However, although the growth of the internal boundary layer due to sea breeze circulation has been clarified to a considerable extent, the role of the variable land and sea surface of inter-tidal zones remains unclear.

The objective of the present study is to observe the land and sea surface-atmosphere interaction over the inter-tidal zone of the Ariake Sea.

2. FIELD OBSERVATION AND SITE CHARATERISTICS

An automated weather station (AWS; Photo 1) deployed in the inter-tidal zone near Kumamoto Port (Fig. 2). The site is located approximately 600 m to the west of the Kumamoto Plane shoreline and 200 m north of Kumamoto Port (Yumesaki Island) (32°46'5" N, 130°35'40" E). The mouth of the Shira River is located approximately 1.0 km northeast of the AWS. In this region, the surface is exposed to about 1.5 km offshore at the lowest water level. In the immediate vicinity of the spring tide, but remains submerged at the neap tide. Land and sea breezes are generally observed on a diurnal cycle (Fig. 3), where the sea breeze (260–320°) is dominant during the day, and the land breeze (~90°) is dominant at night. The significant wave height takes as high as several centimeters usually condition, however, it becomes as high as 80 cm (25 – 30 % of the high water level) on the passing the severe storm (Fig. 4 and 5).

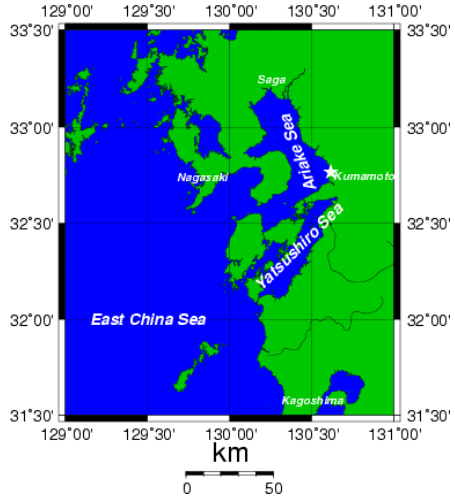

Fig. 1 Location of the Ariake Sea to the west of Kyushu Island

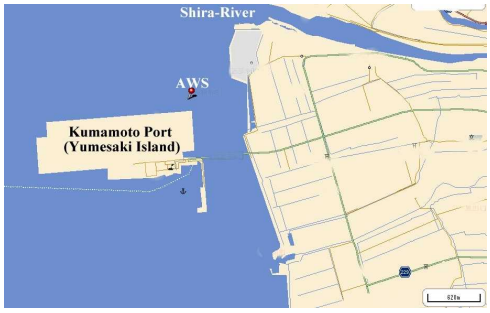

Fig. 2 Location of the Automated Weather Station (AWS) near the Kumamoto Port

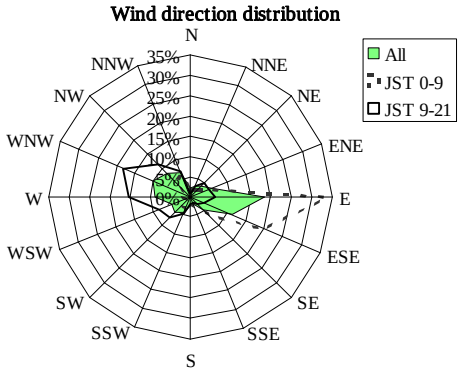

Fig. 3 Wind direction chart observed at the AWS. All represents the all of 30-minute average data, JST 0-9 (JST: Japan Standard Time = UTC + 9 hrs.) are the wind direction during midnight and morning. JST 9-21 are the direction during daytime and early night.

* Corresponding author address: Kenji Tanaka, Kumamoto Univ., Dept. of Civil and Environmental Engineering, Kurokami 2-39-1, Kumamoto, 860-8555, Japan; E-mail : ktanaka@gpo.kumamoto-u.ac.jp

The turbulence flux measurement system are composed of a sonic anemo-thermometer (81000, YOUNG) and an infrared H_2O/CO_2 gas analyzer (LI-7500, Li-Cor) on the top of the tower above 10 m from the tidal bottom surface to observe the atmospheric turbulence. The data are sampled at 10 Hz and stored on the data logger (CR-5000, Campbell) with the use of compact flash card.

A four-component radiation sensor was installed to observe the surface radiation budget based on measurements of the upward and downward component of shortwave and longwave radiation flux. Meteorological variable of air temperature, relative humidity and barometric pressure and precipitation are also measured. Those variables are sampled at 5 s intervals and recorded data as 10 min averages. The data stored by the CR-10X were acquired automatically on a daily basis by telemetry using a mobile phone connected to the logger.

In addition to the meteorological observation, basic variables of water quality such as dissolved oxygen (DO), pH, oxidation-reduction potential (ORP), and electric conductivity (EC) were deployed near the tidal bottom surface and have been measured since July 2005. For the water level measurement, a submergible pressure sensor (PTX 1830, Druck) was installed on July 2005 and included to the turbulent measurement system in order to analyze the interaction of the wave characteristics.

Photo 1: The automated weather station on the tidal zone.

Photo 2: Turbulent measurement sensors on the top of the tower.

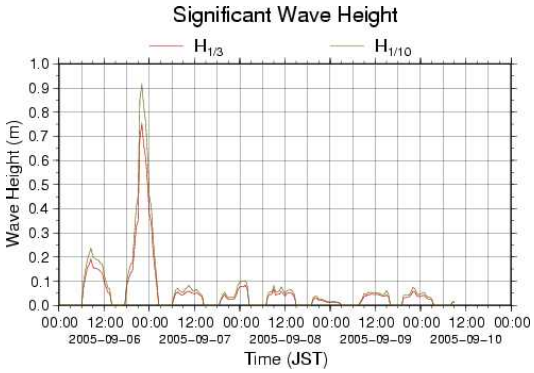

Fig. 4 Diurnal variation of the significant wave height. $H_{1/3}$, $H_{1/10}$ represent one-third and one-tenth (10%) highest wave, respectively.

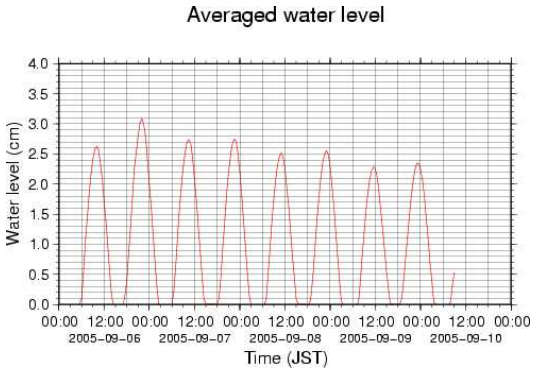

Fig. 5 Diurnal variation of mean water level

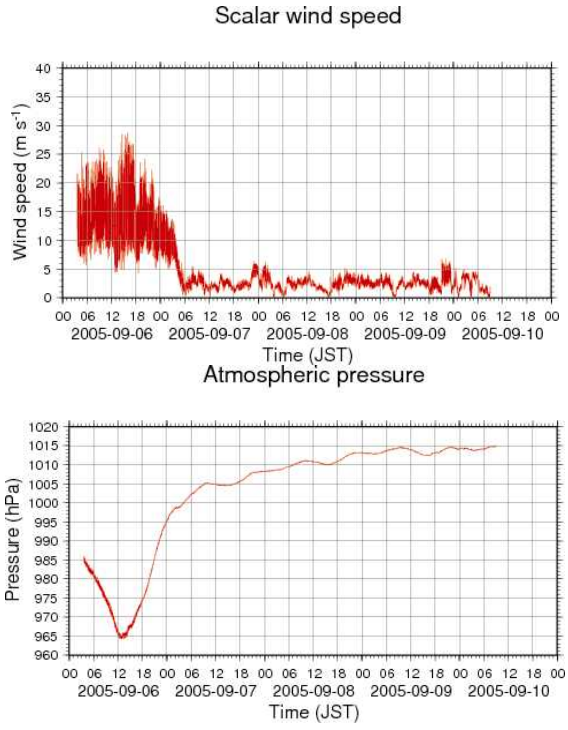

Fig. 6 Variation of wind speed (upper) and pressure (lower) during and after the typhoon attack (T0514).

3. TURBULENT CHARACTERISTICS

3.1. Data process

To obtain the turbulent statistics value from the sampled wind, temperature and humidity dataset, several correcting and filtering processes are required. The air temperature, measured by the sonic anemo-thermometer, was corrected with respect to the traverse wind and specific humidity q by

$$T_{SV} = T_S(\text{uncor}) + \frac{V_n^{\,2}}{403} \tag{1}$$

$$T = T_{SV}\left(1 - 0.514q\right) \tag{2}$$

Kelvin after correction for horizontal wind, T_S(uncor) is the temperature before correction, and V_n is the horizontal wind speed after translating the coordinate system accounting for the axis of the main stream direction.

3.2. Similarity of second order momentum

According to the Monin-Obukhov similarity theory any dimensionless characteristic of turbulence is dependent only upon z/L, as given by

$$\frac{z}{L} = \frac{\kappa g z T_*}{Tu_*^{\,2}} = -\frac{\kappa g z \overline{w'T'}}{Tu_*^{\,3}} \tag{3}$$

where κ is the von Kármán constant (= 0.40), g is the acceleration of gravity (= 9.8 ms^{-2}), z is the measurement level of the surface, T is the mean air temperature in Kelvin, u_* is the friction velocity, and T_* is the temperature scale. The friction velocity, temperature scale and humidity scale (q_*) are defined

$$\begin{aligned} u_*^{\,2} &= -\left(\overline{u'w'}\right) \\ T_* &= -\left(\overline{w'T'}\right)/u_* \\ q_* &= -\left(\overline{w'q'}\right)/u_* \end{aligned} \tag{4}$$

where overlines denote time averages and primes de note the turbulent fluctuation from the average.

In the inter-tidal zone, the measurement level from the surface varies according to the water level. In this study, the stability parameter $\zeta$is defined in terms of the mean water level $\tilde{\eta}$ as

$$\zeta = \frac{z - \tilde{\eta}}{L} \tag{5}$$

where z (= 10 m) is the measurement level from the sea-bottom surface. For a more exact definition, the aerodynamic surface roughness length z_{0m}, zero plane displacement d due to wave motion, or some factor indicating the trend of the water level should be included in ζ. However these factors are sufficiently smaller than $z - \tilde{\eta}$ and to be considered negligible.

Fig. 7 shows the histogram of the stability parameter ζ for every 30-minute data. During the night, the stratification On the land surface condition, Fig. 7 shows a scatter plot of the nondimensional standard deviation of the horizontal wind (in the main stream direction) and the vertical wind versus the stability parameter ζ. All 30-minute dataset observed data are plotted.

Fig. 8 shows the nondimensional standard deviation of the vertical wind, temperature and specific humidity. The nondimensional standard deviation of vertical wind σ_w/u^* was in good relationship with the stability parameter ζ as well as the past studies observed on land surfaces. However, the temperature and specific humidity exhibit large scatter in both the stable and unstable conditions, although a decreasing trend can be seen at high instability of stratification. This wide scatter appears to be due to horizontal heterogeneity of the scalar constituent due to surface characteristics in the vicinity of the site.

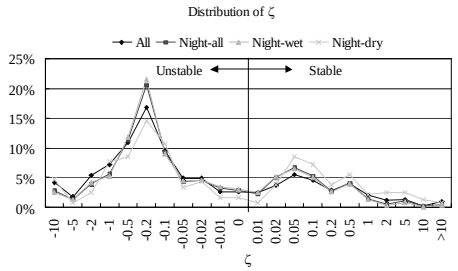

Fig. 7 Frequency distribution of stability parameter ζ, where 'All' denotes all data, 'Night-all' denotes data obtained in the period 2000–0600 JST, 'Night-wet' denotes data obtained when the water level was higher than 0.1 m, and 'Night-dry' indicates data obtained when the water level was lower than 0.1 m.

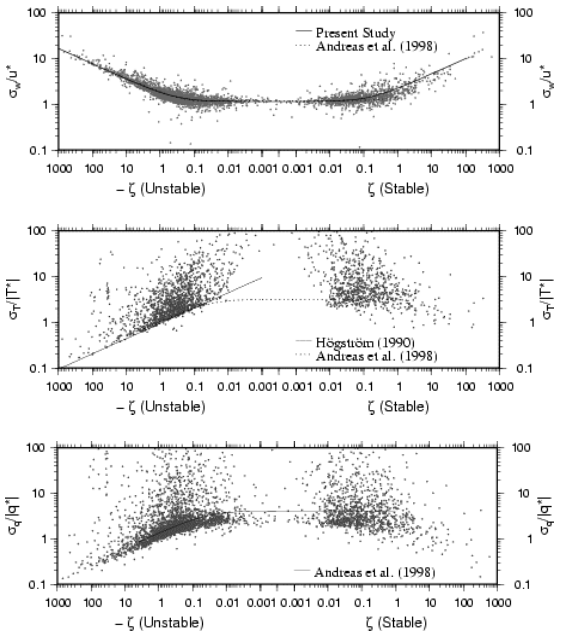

Fig. 8 Scatter plot of the nondimensional standard deviation of vertical wind (upper panel), atmospheric temperature (middle panel) and specific humidity (lower panel) versus stability parameter ζ

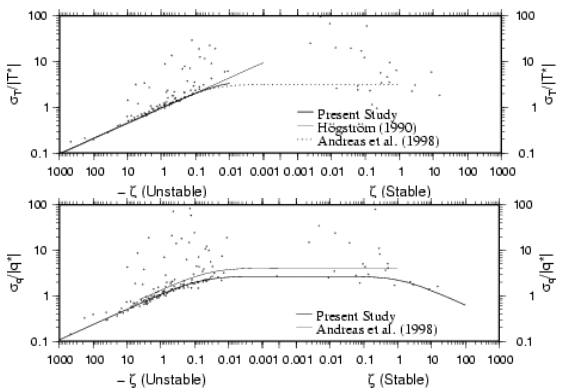

Fig.9 Similar as Fig.8 but of the air temperature (upper panel) and specific humidity (lower panel) after selected data with the wind from offshore (260-330 deg.) and water level lower than 0.01 m.

Fig. 9 shows the nondimensional standard deviation of temperature and specific humidity under the condition of sea breeze (260-330 deg) exposed surface. Without some exception, the nondimensional standard deviation of humidity looks following the –1/3 power functional relationship with ζ. From the plots, the best-fit function of $\sigma_q/|q^*|$ is

$$\frac{\sigma_q}{|q_*|} = \begin{cases} 2.7(1-15.5\zeta)^{-1/3} & (\zeta \le 0) \\ 2.7(1+0.8\zeta)^{-1/3} & (\zeta > 0) \end{cases} \quad (6)$$

The neutral condition of $\sigma_q/|q_*|$ in this study (= 2.7) is smaller than that of Andreas et al. (1998) ($\sigma_q/|q_*| \sim 4.1$), implying that the correlation $R^2 = (u^*q^*)^2/\sigma_w^2\sigma_q^2$ in the inter-tidal zone under sea breeze conditions is stronger (closer to unity) than over the land surface.

4. ENERGY FLUX

Fig. 10 and 11 show the diurnal variation of the atmospheric surface energy flux of net radiation, sensible heat and latent heat during the summer and autumn, respectively. Diurnal variation of the heat flux into the tidal bottom soil and water level are also shown in the same figures. In the daytime, the latent heat flux increases gradually as the water level decreases. As soon as the tidal bottom surface is exposed, the latent heat flux increases as high as 500 W m^{-2} on the fine weather during summer, or as high as 300 Wm^{-2} during autumn. During the night, the latent heat flux still becomes as high as several tens W m^{-2} and sometime exceeds to 100 W m^{-2}.

Exposed hours during the daytime strongly control the latent heat flux. In the Fig. 11, the tidal bottom surface began to expose from 1330 JST to 1500 JST,

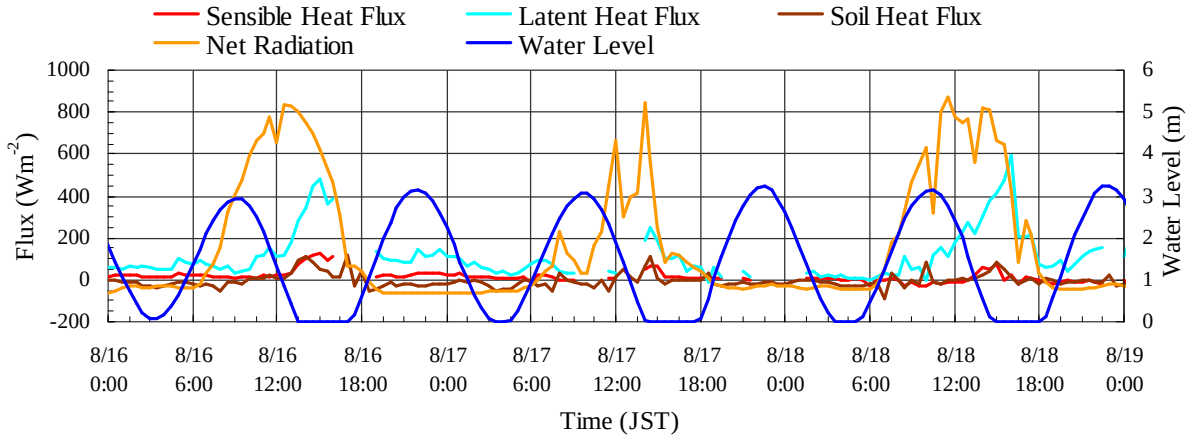

Fig. 10 Diurnal variation of atmospheric surface energy flux (net radiation, sensible heat and latent heat), soil heat flux and water level between 16 and 18, Aug., 2004.

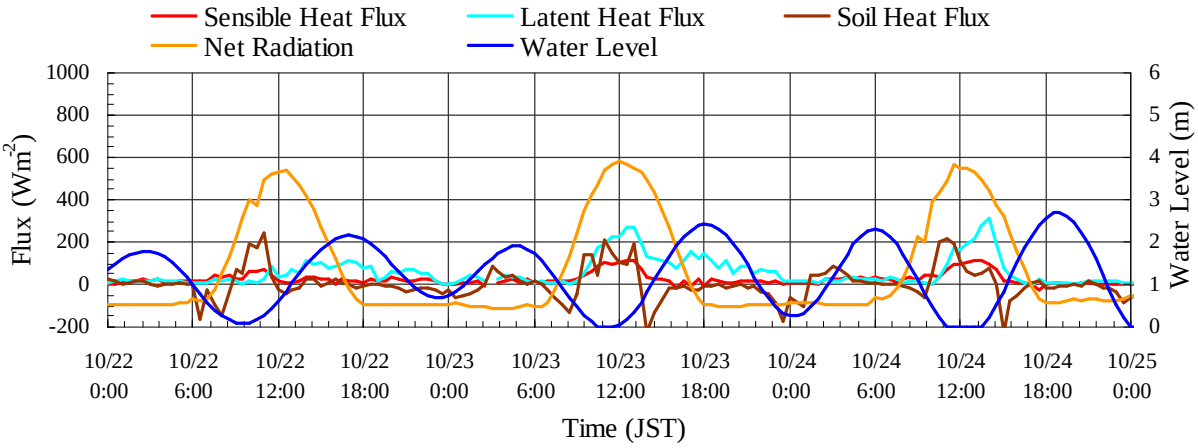

Fig. 11 Same as Fig. 10, but between 16 and 18, Aug., 2004.

and the most of the net radiation came to share the latent heat flux within a couple of hours during exposition. However, when the surface is exposed during the morning, the sensible heat flux does not increase so much. For example shown in Fig. 11, the surface exposed from 1000 JST to 1200 JST on 23 Oct 2004 and the latent heat fluxes increased as high as 200 – 270 W m^{-2}, about an 1/3 or less than half of the net radiation. On Oct. 24, on the other hand, the exposed hour was 1 hour later than that on the previous day, and the duration time of exposition was more extended by 1 hour than the previous day. The latent heat flux on Oct. 24 became higher than that on 23rd. The maximum latent heat flux exceeded to 300 W m^{-2} and as high as 2/3 of net radiation.

Fig. 12 and 13 show the diurnal variation of tidal bottom soil temperature, surface skin temperature, and air temperature according to the tidal motion in the summer and autumn, respectively. The surface skin temperature is derived from the longwave radiation using following equation

$$T_{skin} = \left[\left(L^{\uparrow} - (1-\varepsilon_s) L^{\downarrow} \right) / \varepsilon_s \sigma \right]^{1/4} \quad (7)$$

where L represents the longwave radiation flux, ε_s is the emissivity of surface, and s is the Stefan-Boltzman constant (=5.67×10^{-8} W $m^{-2}K^{-4}$), respectively. Hence the T_{skin} represent the skin temperature of the sea surface under submerged condition and that of the tidal bottom surface under exposed condition. During the daytime, the near surface soil temperature increases more than 5 degC during exposed surface. The diurnal range of soil temperature became less than 1 degC at 30 cm below the tidal bottom surface. The atmospheric temperature was lower than surface skin temperature throughout these periods, except on 18 Aug, 2004. That is, the atmospheric bulk Richardson number took negative mostly and stratification was unstable both day and night.

During the exposed hours, the present results looks satisfied well the simple surface energy balance equation

$$Rn - G_0 = H + lE \quad (8),$$

where G_0 represents the tidal bottom soil heat flux into deep soil layer. During the submerged condition, however, it is required to consider the net heat storage

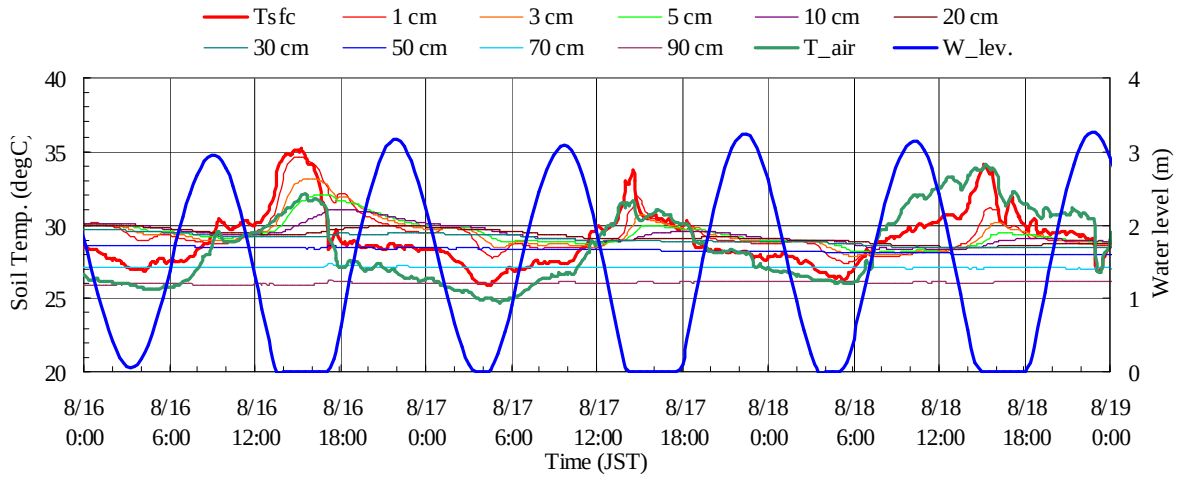

Fig. 12 Diurnal variation of the tidal bottom soil temperature, surface skin temperature from longwave radiation , and atmospheric temperature (above 7.2 m from tidal bottom surface) with the comparison to that of water level, between 16 and 18 Aug. 2004.

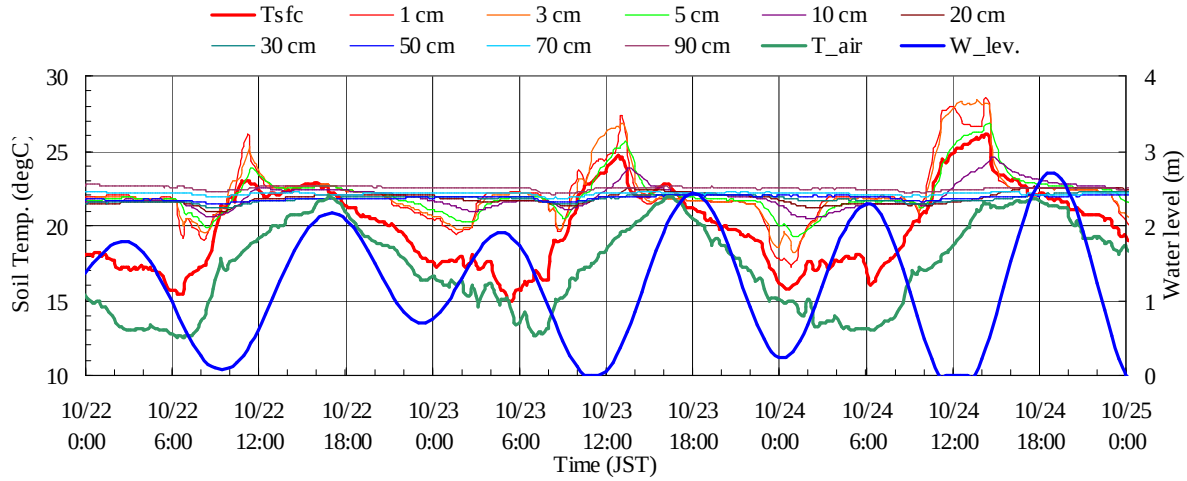

Fig. 13 Same as Fig. 12 but between 16 and 18 Aug. 2004.

of the seawater, which discuss later.

5. DISCUSSION

The conservation equation of the seawater temperature T_w can be written as

$$\frac{\partial T}{\partial t} + u_i \frac{\partial T}{\partial x_i} = \frac{\partial}{\partial x_i}\left(K_i \frac{\partial T}{\partial z_i} \right) + \frac{Q_{in}}{\rho_w c_w} \tag{9}$$

The vertical integrated form of Eq. (9) yieds

$$\int_0^h \rho_w c_w \frac{\partial T}{\partial t} dz + \int_0^h \rho_w c_w \left[u \frac{\partial T}{\partial x} + v \frac{\partial T}{\partial y} + w \frac{\partial T}{\partial z} \right] dz$$
$$= \int_0^h \rho_w c_w \left[\frac{\partial}{\partial x}\left(K \frac{\partial T}{\partial x} \right) + \frac{\partial}{\partial y}\left(K \frac{\partial T}{\partial y} \right) + \frac{\partial}{\partial z}\left(K \frac{\partial T}{\partial z} \right) \right] dz + Q_{sfc} - G_0 \tag{10}$$

Substituting the typical value for each variables and coefficients: the seawater density r = 1.025×10^3 kg m^{-3}, c=4.00×10^3 J kg^{-1}, DT/dt=0.2/3600 K s^{-1}, u~±0.2 m s-1, w_{sfc}= dh/dt ~ ±0.5/3600 m s-1, DT/dx ~ 1.0×10^{-4} K m^{-1}, DZ/Dt = 1.0 K m^{-1}, z = 0~3 m, respectively. The first tem of left hand side takes 0~6.6×10^2 W m^{-2}, the second term of left hand side takes 0~2.43×10^2 W m^{-2} for horizontal current and 0~5.5×10^2 for vertical tidal motion. Each component of the sea water temperature equation is as the same order or little bit higher in magnitude than Q_{sfc} and G_0. Therefore, in the coastal zone including the tidal flat, not only the horizontal gradient of temperature (advection term) but the column heat storage and apparent heat storage due to tidal motion (last term of left hand side) plays important role for the atmospheric surface energy budget.

6. SUMMARY

In the tidal zone, the land and seawater cover conditions changes periodically mainly according to the tidal cycle, which makes the cycle of the energy flux variation more complicated. The exposed hours in daytime controls the heating of the tidal bottom surface and then the increasing of the latent heat flux and the sensible heat flux. The latent heat flux becomes highest under the condition that the tidal bottom surface exposed during the afternoon and the seawater submerges again in the evening. In the present result, the maximum value became as high as 500 Wm^{-2} on summer fine weather., and during the night the latent heat sometimes exceeded to 100 W m^{-2}.

During the submerged condition, the column heat storage of seawater and the heat exchange by horizontal advection or tidal motion (column mass exchange) have a highly possible to control the latent heat and sensible heat flux according to the brief scale analysis.

ACKNOWLEDGEMENT

This study was supported by a grant from Japan Society for the Promotion of Science (Scientific research A-2-1420872). This study was also supported by a grant from Ministry of Education Culture, Sports Science and Technology (Grant-in-Aid for Young Scientists B-17710016).

REFERENCES

Andreas, E.L., Hill, J.R., Gosz, J.R., Moore, D.L. Otto, W.D., and Sarma A.D., 1998: Statistics of surface-layer turbulence over terrain with meter-scale heterogeneity, Boundary-Layer, Meteor., **86**, 379-408.

Garatt, J.R., 1994: The Atmospheric Boundary Layer, Cambridge University Press.

Högström, U., 1990: Analysis of turbulence structure in the surface layer with a modified similarity formulation for near neutral conditions, J. Atmos. Sci. **49**, 1949-72.

Kadar, B.A. and Yaglom A.M., 1989: Mean fields and fluctuation moments in unstably stratified turbulent boundary layers, J. Fruid Mech., 212, 637-662

Kruit, R.J.W., Holtslag, A.A.M., and Tijm, A.B.C, 2004: Scaling of the sea-breeze strength with observations in the neatherlands, Boundary-Layer Meteor., **112**, 369-380.

Lange, B., Larsen, S., Højstrup, J., and Barthelmie, R., 2004: The influence of thermal effects on the wind speed profile of the coastal marine boundary layer. Boundary-Layer Meteor., **112**, 587-617.

Plant, R.S., and Atkinson B.W., 2002: Sea-breeze modification of the growth of a marine internal boundary layer. Boundary-Layer Meteor., **104**, 201-228.

Tanaka, K., A. Narimatsu, K. Morimoto and K. Takikawa, 2005: Turbulent characteristics of the atmospheric surface layer in the inter-tidal zone of the Ariake sea, Asian and Pacific Coasts 2005, Sep. 4-8, 2005, Jeju, Korea, 1816-1829.